Development of a new Phobos spectral simulant: spectral properties from visible to the mid-infrared range

Antonin Wargnier, G Poggiali, A Doressoundiram, Thomas Gautier, P Beck, A Buch, N Ruscassier, S Fornasier, M A Barucci

To cite this version:

Antonin Wargnier, G Poggiali, A Doressoundiram, Thomas Gautier, P Beck, et al.. Development of a new Phobos spectral simulant: spectral properties from visible to the mid-infrared range. Monthly Notices of the Royal Astronomical Society, 2023, 524 (3), pp.3809-3820. ⟨10.1093/mnras/stad2132⟩. ⟨hal-04191010⟩

HAL Id: hal-04191010

https://hal.sorbonne-universite.fr/hal-04191010v1

Submitted on 30 Aug 2023

Development of a new Phobos spectral simulant: spectral properties from visible to the mid-infrared range

Antonin Wargnier,[1,2★] G. Poggiali,[1] A. Doressoundiram,[1] T. Gautier,[2,1] P. Beck,[3] A. Buch,[4]
N. Ruscassier,[4] S. Fornasier,[1,5] and M. A. Barucci[1]
[1]*LESIA, Observatoire de Paris, Université PSL, CNRS, Sorbonne Université, Université de Paris-Cité, 5 place Jules Janssen, 92195 Meudon, France*
[2]*LATMOS, CNRS, Université Versailles St-Quentin, Université Paris-Saclay, Sorbonne Université, 11 Bvd d'Alembert 78280 Guyancourt, France*
[3]*Univ. Grenoble Alpes, CNRS, IPAG, 38000 Grenoble, France*
[4]*Laboratoire Génie des Procédés et Matériaux, CentraleSupélec, Université Paris-Saclay, Gif-sur-Yvette, France*
[5]*Institut Universitaire de France (IUF), 1 rue Descartes, F-75231 Paris Cedex 05, France*

Accepted 2023 July 11. Received 2023 July 4; in original form 2023 March 24

ABSTRACT

Phobos is the target of Martian Moons eXploration (MMX) the next sample return mission of the Japanese space agency (JAXA). The mission will investigate the origin of Phobos and Deimos – the two martian moons, using a suite of dedicated instruments. Infrared analysis of the surface composition will be performed by the MIRS spectrometer onboard MMX.

Within the scientific studies performed in preparation of the mission, we developed a new laboratory spectral simulant that well reproduces the red and featureless spectrum of Phobos. Our results show that a visible and near-infrared simulant can be developed using dark opaque materials such as anthracite and coal to reduce the reflectance and absorption features. To investigate the reliability of our proposed simulant in terms of composition and mineralogy we discussed the similarities and differences in the mid-infrared (MIR) range between our laboratory simulant and some past observations acquired on Phobos. Spectra with different observation geometries were also acquired for our simulant which gives information about grain size and textures of the surface. The simulant developed in our study presents a better match for the Phobos spectrum in the visible and near-infrared compared to the previously proposed simulants.

Key words: Methods: laboratory: solid state – Planets and satellites: individual: Phobos – Planets and satellites: surfaces – Planets and satellites: composition

1 INTRODUCTION

1.1 Context

Several in situ and ground-based observations have shown that Phobos and Deimos – the two martian moons – are small bodies respectively of about 27 and 15 km, highly processed, cratered, with a red and flat near-infrared spectrum (Murchie & Erard 1996; Murchie 1999; Rivkin et al. 2002; Fraeman et al. 2012, 2014; Pajola et al. 2012, 2018; Takir et al. 2022). These peculiar characteristics for a moon in the Solar System led to suppose that Phobos and Deimos could be D-type asteroids captured from the main asteroid belt (Rivkin et al. 2002; Fraeman et al. 2014). A second theory has been proposed to explain the orbital parameters such as inclination and eccentricity that the first hypothesis failed to justify. In this case, a collision between Mars and a protoplanet may have created the two martian moons (Craddock 1994, 2011; Rosenblatt et al. 2016; Hyodo et al. 2018). The discrepancy on the origins of Phobos and Deimos will be addressed by the future JAXA Martian Moon eXploration (MMX) sample-return mission (Kuramoto et al. 2022).

In this work, we will present the updates of the simulant proposed in Wargnier et al. (2023) and the comparison with existing spectroscopic data of this new laboratory spectral simulant of Phobos, in support of the entire MMX mission. In particular, the development of this new simulant will be pivotal for the calibration and future data interpretation of the MMX Infrared Spectrometer (MIRS, Barucci et al. 2021). Moreover, the analysis made on simulant samples will be important also for other experimental and spectral studies of Phobos.

Phobos, the main target of MMX mission, presents two different surface units: the so-called "red" and "blue" units (according to near-infrared observations) that possibly correspond to different surface ages. In this work, we focused on a possible red unit simulant, as this unit corresponds to the largest part of the Phobos' surface, whereas the blue unit is mostly concentrated around the Stickney crater, the biggest crater on Phobos with a diameter of 9 km.

1.2 Phobos laboratory simulants

Nowadays, no analog material or simulant achieved a perfect match of Phobos spectra in terms of slope in the near-infrared nor features in the mid-infrared (Fraeman et al. 2012; Miyamoto et al. 2021; Landsman et al. 2021; Poggiali et al. 2022; Wargnier et al. 2023). The University of Tokyo developed two simulants (UTPS,

---

★ E-mail: antonin.wargnier@obspm.fr

Miyamoto et al. 2021) based on the different hypotheses on Phobos origin. These simulants reproduce mineralogical properties including particle-size distributions, packing density, and mechanical properties. UTPS analogs are reasonable simulants for optical characteristics of Phobos surface with a spectral slope in the near-infrared close to the slope of Phobos. Our previous study (Wargnier et al. 2023) started a process of improvement of the spectral match in the near-infrared with data collected on Phobos. The reflectance level and the spectral slope in the near-infrared match well with the Phobos red-unit simulant; but the change of slopes between visible and near-infrared was not reproduced.

A spectral match in the visible and the near-infrared between the Phobos spectrum and a mixture of different materials is, of course, not an affirmation that Phobos is composed of the same elements as the mixture. Because the Phobos spectrum is mostly featureless, with potentially a faint absorption band in the 3 µm region (Fraeman et al. 2014), a clear understanding of its composition is difficult and several mixtures can well reproduce this type of spectra. From the few observations in the thermal infrared, spectral features are more important in this wavelength region.

We present in this work a spectro-photometric simulant of Phobos in the visible and the near-infrared but, for a better understanding of the mineralogical aspects, we measured and compared the mid-infrared reflectance spectra of the simulant with the available Phobos spectra in the MIR from Giuranna et al. (2011) and Glotch et al. (2018).

2 MATERIALS AND METHODS

2.1 Endmembers for the development of the Phobos simulant

The choice of materials is pivotal in simulant development studies. Based on previous observations, Phobos could be close to a D-type asteroid, therefore we have tried to produce the simulant as more representative as possible of the potential composition of a small body. This type of primitive asteroid usually found in the outer main belt such as in the Hilda group, or in the Jupiter trojans is characterized by a very low albedo and a featureless red spectrum. They might be composed of organics, silicates, carbon, and possibly water ice in the interior (Fanale & Salvail 1989; Fanale & Salvail 1990; Pätzold et al. 2013). For the silicate part, we chose to use olivine ($(Mg,Fe)_2SiO_4)$) which has been detected on several asteroids. Olivine used in this study was retrieved from Brazil (Wargnier et al. 2023). We used coals to mimic the carbon- and organic-rich compounds in our Phobos simulant. In addition to the interest of representativeness by using coals, they are really helpful to decrease the reflectance level to reach the value of Phobos with an albedo of roughly 7% at 550 nm (Avanesov et al. 1991; Thomas et al. 1999). These opaque materials and their effects have been largely studied in the literature (Singer 1981; Cloutis et al. 1990a,b). The dark component in our simulant is represented by anthracite and DECS-19. Anthracite is a mature coal with 91.9% carbon while DECS-19 is composed of 85.6% carbon (Vinogradoff et al. 2021). In addition to anthracite and DECS-19, we tested also iron sulfide as a darkening agent for its great darkening effect with respect to other compounds. Anthracite and iron sulfide were provided and prepared by the Institut de Planétologie et d'Astrophysique de Grenoble (IPAG, France) while DECS-19 was purchased from the Penn State Coal Sample Bank (Vinogradoff et al. 2021). The reader can refer to Wargnier et al. (2023) for additional details about the components characteristics and their representativeness in the context of primitive asteroids.

Table 1. Composition of the prepared mixtures in olivine, anthracite, DECS-19, and iron sulfide. Quantities are given in vol.%.

Mixtures	**Olivine** Grain size 2 µm	**Anthracite** Grain size <1 µm	**DECS-19** Grain size 3 µm	**Iron sulfide** Grain size <1 µm
1	65	20	15	–
2	63	22	15	–
3	63	20	17	–
4	61	22	17	–
5	59	24	17	–
6	60	20	20	–
7	59	22	17	2
8	58	20	22	–
9	56	22	22	–

2.2 Preparation of samples and mixtures

Olivine and anthracite were grounded and sieved to obtain a powder. The grain size distribution was then determined more accurately using SEM images, as reported in Sect. 2.3. Powders of each endmembers were weighed separately with a precision of 0.1 mg to reach the needed volume fraction in the mixture. To enable these volume fraction mixtures, volume quantities were converted to mass using density values from literature. For the olivine, we used the mean value (3.3 g.cm−3) suggested in different papers for magnesium-rich olivine (e.g., Flinn 1983; Koike et al. 1993; Sultana et al. 2023). For iron sulfide (4.82 g.cm−3) and anthracite (1.62 g.cm−3) sample, the values were measured in Sultana et al. (2023) using respectively a pycnometer and the liquid displacement technique. The density of DECS-19 (1.75 g.cm−3) was taken using the centered value of the density interval given by Vinogradoff et al. (2021). The powder of the different members was then mixed together with a clean agate mortar for 5 min by hand, with a pestle, in order to obtain an intimate mixing. Our intimate mixing method decreases a bit the grain size of the different endmembers. We are unable to quantify the decrease of the grain size. We prepared mixtures with different volume percentages of each component. The composition of the mixtures is given in Table 1. Initial volume fraction was chosen accordingly to the work presented in Wargnier et al. (2023) and then fractions were modified by a few percent between mixtures, in particular for anthracite and DECS-19. Small modifications were necessary because of the large effect on the red slope of the DECS-19 in the VNIR and of the important darkening power of hyperfine anthracite. Only 2 vol.% can change the reflectance level by 1%.

2.3 SEM images and energy-dispersive X-ray spectroscopy

Scanning Electron Microscopy (SEM) studies were conducted at the Laboratoire de Génie des Procédés et Matériaux (LGPM, France). Samples were placed on a double-sided carbon tape. We performed secondary electron imaging with a FEI Quanta200 environmental SEM at 12 or 15 kV depending on the material, and magnification between 250 and 4000 for each end member, in low-vacuum mode. SEM images were used to derive the grain size distribution of the different endmembers used in this work (olivine, anthracite, and DECS-19), but also to study the mixture prepared (see Sect. 3.3), which is particularly crucial because it has an important impact on the final spectrum.

Grain size distribution was derived using the ImageJ software (Schneider et al. 2012). In order to obtain a representative sample of olivine, we counted the grains on images with low magnification

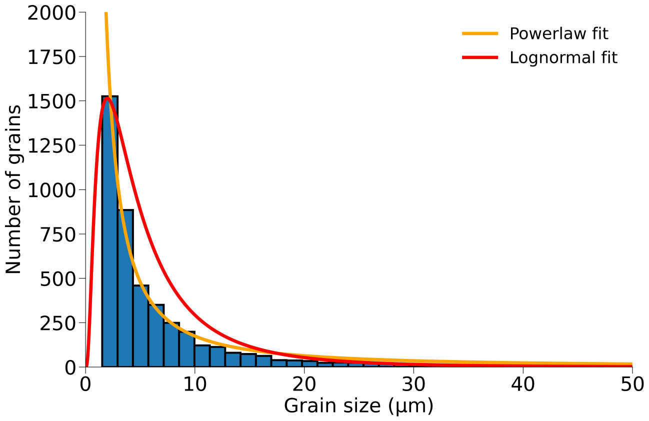

Figure 1. Grain size distribution of olivine. The grain size is the Feret's diameter computed using SEM images. The red curve is the lognormal distribution fit to the data. The orange line represents the power-law fit to the data.

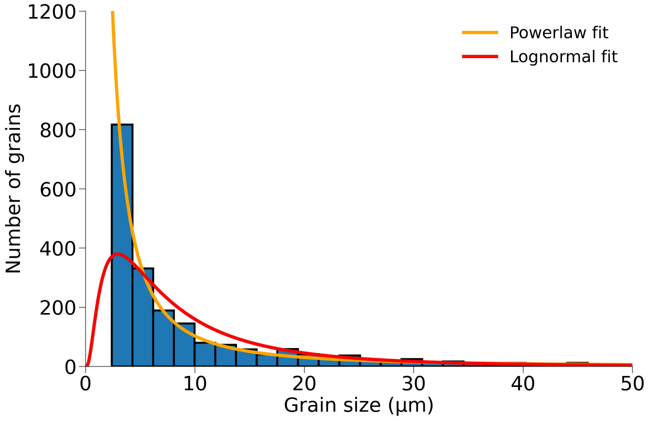

Figure 2. Grain size distribution of DECS-19. The grain size is the Feret's diameter computed using SEM images. The red curve is the lognormal distribution fit to the data. The orange line represents the power-law fit to the data.

(x250). We computed the Feret's diameter – size of the grain in one specified axis – of each grain visible in the images (e.g., Just et al. 2020; Sultana et al. 2021). Because a pixel on the image is roughly 1 µm, sub-micrometer grains cannot be measured and we used a threshold of 2 pixels to count and measure the grains in order to avoid artifacts in the images. Cumulative grain size distributions obtained with this method are given in Fig. 1 and Fig. 2. More than 4500 olivine grains were measured to allow sufficient statistics. For DECS-19, we counted more than 2000 grains. On Figs. 1 and 2, grain size distributions are plotted from 0 to 50 µm. Some olivine and DECS-19 grains are larger than 50 µm but represent about 50 grains in the thousand grains measured. Olivine and DECS-19 maximum grain sizes are respectively 220 µm and 380 µm. Smaller grains are probably underestimated due to fine grains stuck on larger grains which we were not able to measure using this method. Grain size distributions for the iron sulfide and anthracite were already derived in Sultana et al. (2023). Hence, the following discussion will be dedicated to olivine and DECS grain size distribution.

Planetary bodies are generally found to be covered by fine-grained regolith following a power law grain size distribution function (Buhl et al. 2014). Hence, a power law fitting ($N = Ad^{-B}$, where N is the occurrence, d the grain diameter, and A and B the power law parameters) of the data was performed and gives the following best-fit parameters for the olivine: $A = 5020 \pm 301$ and $B = 1.46 \pm 0.05$. For the DECS-19, we found $A = 5908 \pm 83$ and $B = 1.76 \pm 0.01$. Because we don't have data for small grains (< 2 µm) a lognormal fitting of the data was also performed according to previous works (e.g., Toriumi 1989; Sakatani et al. 2018; Simon et al. 2018; Sultana et al. 2023) and gives the most probable value of grains size. For the olivine, grains are mainly around 2 µm and for DECS the grains have a most probable size of 3 µm. In the following, the grain size of olivine and DECS will be stated according to these most probable values given by the peak position of the lognormal distribution. DECS appears to have a larger distribution than olivine, with more grains bigger than 50 µm. The power law indices and the lognormal best-fit parameters (μ, σ) are quite similar for the two endmembers and indicate that for olivine and DECS-19, the grain size distributions are dominated by fine grains. Therefore, their mixture in the final analog mixture is a good representative of regolith-cover surfaces like Phobos. Moreover, the distribution of the grain size of our endmember is largely below 150 microns as suggested for Phobos by thermal inertia measurements (Lunine et al. 1982). Presence of a transparency feature observed on Phobos spectra (Glotch et al. 2018) is also in agreement with a < 50 microns dominated mixtures as well for the mean value of grain sizes in our samples.

Table 2. Ratio of the different components in the olivine sample. Values are obtained and averaged on 8 different grains of olivine. The elements are ordered by abundance.

Elements	Weight (%)	Atomic (%)
Mg	30.3	26.4
Si	19.7	14.8
Fe	7.7	3.0

Moreover, we investigated the chemical elementary composition with energy-dispersive X-ray spectroscopy (EDX) using an EDAX Metek New XL30. EDX analysis conducted in this work allows to evaluate the Mg/Fe content in our olivine. The analysis was performed on several grains of the olivine (Table 2). EDX analysis of the different olivine grains shows only slight variations up to ± 3%. Our olivine is mostly composed of magnesium, then silicon. It presents also a small part of iron. The composition given by the EDX highlights the fact that our olivine is a magnesium-rich olivine (forsterite).

2.4 Reflectance measurements

We performed bidirectional reflectance measurements using different instruments according to the wavelength range investigated. Bidirectional measurements were commonly used in planetary science laboratory experiments (e.g., Bishop et al. 1994; Brucato et al. 2010; Takir et al. 2019; Beck et al. 2021; Sultana et al. 2021; Potin et al. 2022) and allow a better comparison with data obtained by space missions. For the visible and near-infrared, we used the Spectrophotometer with cHanging Angles for Detection Of Weak Signals (SHADOWS) at IPAG. SHADOWS is composed of two detectors (Potin et al. 2018): a silicon detector measures the visible part of the spectrum (0.4-1.0 µm), and an InSb detector cooled at 77K is used for the near-infrared (1.0-4.2 µm). Reference measurements were performed with a Spectralon® (Labsphere) for the visible range and with

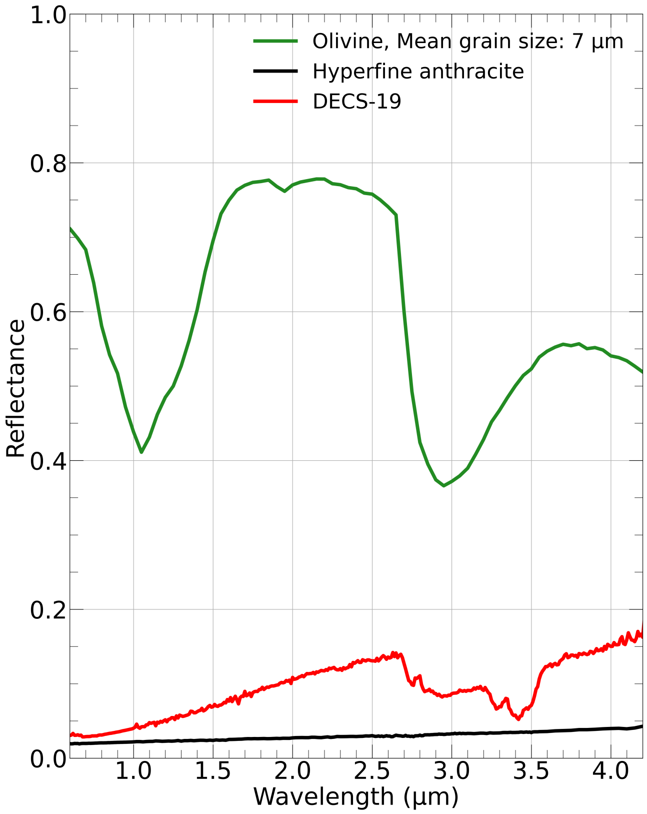

Figure 3. SHADOWS spectra of the different endmembers used in this study, from 0.6 µm to 4.2 µm.

an Infragold® (Labsphere) for the near-infrared range. The absolute photometric accuracy of the instrument is 1% (Potin et al. 2018). Spectral parameters such as spectral sampling and spectral resolution are reported in Appendix A (Fig. A1). SHADOWS allow also to measure spectra with different geometry of observation, varying the incident, emission, and azimuth angles. The nominal configuration with incidence i = 0°, emission e = 30°, and azimuth ϕ = 30° has been used in the following, unless explicitly stated otherwise.

The mid-infrared bidirectional reflectance spectrum was obtained using a Fourier Transform Infrared Spectrometer (FTIR) Bruker Vertex 70V mounted with the Bruker A513/QA variable angle reflection accessory at IPAG. We scanned a wavelength range between 1.25 to 20 µm (8000 to 500 cm^{-1}). One hundred scans were acquired with a spectral resolution of 4 cm^{-1} in the geometrical configuration i = 0°, e = 30°, ϕ = 0°. Reference measurements were made using Infragold® (Labsphere). The spectrometer is equipped with a MCT detector cooled with liquid nitrogen and with optical elements in KBr.

Fig. 3 shows the spectra of the different endmembers used in this work as seen in Sect. 2.1. Olivine has a reflectance of about 70% and presents an absorption band at 1 µm due to the presence of iron ions (Sultana et al. 2021), and a deep 2.7 µm O-H feature probably due to absorption/adsorption of molecular water in the olivine powder or O-H defect in the structure of olivine. Anthracite is characterized by a red-sloped in all the wavelength ranges of interest, with no absorption band, and a reflectance lower than 0.05 making it the most appropriate darkening factor among the endmembers to reproduce the Phobos spectrum. The DECS-19 shows a strong red-sloped spectrum compared to anthracite, with a reflectance of roughly 0.02 at 0.6 µm and more than 0.1 at 4.2 µm. A broad feature can be observed at 2.7 µm, possibly also due to absorption/adsorption of terrestrial water. We note also the presence of two absorption bands at 3.28 µm and 3.42 µm due respectively to aromatic and aliphatic carbon.

2.5 Analysis of the spectra

Because Phobos has a red-sloped spectrum with no significant features – except a possible faint absorption band at 3 µm detected in Fraeman et al. (2014) – in the visible and near-infrared, we compared Phobos and simulant spectra accordingly to their spectral slope and their reflectance level. The spectral slope was evaluated using a linear fitting and using the formula from Delsanti et al. (2001) for 3 regions of the normalized spectrum: between 720 and 900 nm, between 1.5 to 2.4 µm, and from 3.7 to 4.0 µm. These spectral ranges have been chosen out of absorption features that we have in the different mixtures spectra after 2.5 µm.

3 RESULTS AND DISCUSSION

3.1 The VIS/NIR spectra

Values of the spectral parameters for each mixture are given in Table 3 and associated spectra are presented in Fig. 4. These simulant parameters are compared with the CRISM spectrum spectral parameters (Fraeman et al. 2012). We computed the ratio of the spectral slope between 720 and 900 nm with the spectral slope between 1.5 and 2.4 µm, and the ratio of the reflectance at 600 nm with the reflectance at 1.8 µm. We plotted the first ratio as a function of the second one (Fig. 5). Several mixtures are particularly interesting such as mixtures 2, 3, 4, 6, and 8. However, looking further into the values given in Table 3, shows that mixture 2 has a good spectral slope in the visible, but is quite low in the near-infrared. This problem is even more important for mixture 3, and the reflectance level is less consistent with the CRISM data than for mixture 2. Mixture 4 has a really good spectral slope in both visible and near-infrared and a correct reflectance. However, the spectral slope falls drastically for wavelength between 3.7 and 4.0 µm. With the little data available in this wavelength region, we expect the Phobos spectrum to be red with a spectral slope quite similar to that between 1.5 and 2.4 µm (Rivkin et al. 2002). However, according to Takir et al. (2021), the spectrum between 3 and 4 µm is redder than the part of the spectrum between 1.5 and 2.4 µm, but the latest part of the spectrum has also a poor signal-to-noise ratio (Takir et al. 2022). Mixture 8 shows a really good spectral slope in the visible but quite low in the near-infrared. Finally, mixture 6 seems to be a good compromise between the different parameters studied. Spectral slope and reflectance appear to be well reproduced with the mixture 6 (Fig. 6). In the following, this mixture will be named MIX #6.

The MIX #6 presents a slope in the visible and in the near-infrared that fits better with the CRISM spectrum – in terms of the spectral slope – than previously proposed analogs for the red unit of Phobos such as Tagish Lake or Murchison meteorites (Fraeman et al. 2012). The reflectance level for this mixture appears to be a bit higher than Phobos reflectance level shown by the CRISM data in Fraeman et al. (2012), as visible in Table 3 both the reflectance at 600 nm and 1.8 microns available for our mixture and CRISM data shows a statistically significant difference between observation (0.025 and 0.049, respectively) and laboratory measurements (0.039 and 0.057, respectively). However, we need to take into account the possible

Table 3. Spectral parameters of the mixtures prepared for this study. Comparison with CRISM and UTPS-TB spectral parameters. CRISM and UTPS parameters are derived from spectra respectively in Fraeman et al. (2012) reprojected at the same laboratory geometry and Miyamoto et al. (2021). A hyphen in the Table signifies that there is no data at this wavelength for the observation. Uncertainties on the spectral slope and reflectance measurements for the mixtures are due to SHADOWS uncertainties. The spectral slope is given in %/100nm. MIX #6 is chosen in this work as the best simulant in the VNIR for Phobos. Tagish Lake spectral properties before 900 nm were computed on the extrapolated part of the spectrum.

Mixtures	**Spectral slope** (in %/100nm)			**Reflectance**		
	720-900 nm	1.5-2.4 µm	3.7-4.0 µm	600 nm	1.8 µm	4.0 µm
1	4.94 ± 0.03	2.07 ± 0.09	0.45 ± 0.02	0.040 ± 0.001	0.057 ± 0.001	0.077 ± 0.002
2	5.81 ± 0.03	1.91 ± 0.08	1.84 ± 0.08	0.030 ± 0.001	0.046 ± 0.001	0.067 ± 0.002
3	5.52 ± 0.04	1.82 ± 0.10	1.35 ± 0.05	0.040 ± 0.001	0.056 ± 0.001	0.077 ± 0.002
4	6.63 ± 0.05	2.25 ± 0.07	1.15 ± 0.05	0.035 ± 0.001	0.053 ± 0.001	0.074 ± 0.002
5	3.44 ± 0.02	2.17 ± 0.10	0.99 ± 0.06	0.036 ± 0.001	0.047 ± 0.001	0.069 ± 0.002
6	**5.18 ± 0.02**	**2.24 ± 0.10**	**1.88 ± 0.07**	**0.039 ± 0.001**	**0.057 ± 0.001**	**0.083 ± 0.002**
7	3.99 ± 0.03	2.19 ± 0.12	1.16 ± 0.06	0.036 ± 0.001	0.047 ± 0.001	0.067 ± 0.002
8	7.21 ± 0.06	1.84 ± 0.06	1.79 ± 0.07	0.041 ± 0.001	0.062 ± 0.001	0.085 ± 0.002
9	5.62 ± 0.04	2.38 ± 0.11	1.14 ± 0.07	0.039 ± 0.001	0.056 ± 0.001	0.081 ± 0.003
CRISM	8.78	2.99	–	0.025	0.049	–
Tagish Lake	(5.01)	2.62	1.28	(0.013)	0.020	0.030
UTPS-TB	1.53	1.09	-0.71	0.030	0.037	0.040

differences induced by comparing laboratory and remote sensing data and the absolute photometric accuracy of SHADOWS (1%) could explain such a difference with the CRISM data, anyway MIX #6 presents a very dark appearance with a reflectance of 0.057 at 1.8 µm.

Fig. 6 shows also that MIX #6 has a 2.8 µm feature due to the absorption/adsorption of molecular water as already discussed in Sect. 2.2. It is interesting to note that the 1 µm band due to iron ions in the olivine (see Fig. 3) is completely removed by the opaque materials in the MIX #6 spectrum. The MIX #6 spectrum exhibits two organics bands due to aliphatic and aromatic carbon at 3.28 and 3.42 µm due to the presence of DECS-19 in the mixture. These bands could be expected on Phobos (Wargnier et al. 2023) since no observation of Phobos has covered this spectral region with sufficient signal-to-noise ratio (S/N). The depth of the bands could also decrease with space weathering. In the case of the interstellar medium, Godard et al. (2011) found that aliphatic CHs can be destroyed under space weathering conditions (ion bombardment). But space weathering experimental simulations on meteorites using ion irradiation (Brunetto et al. 2014; Lantz et al. 2015) have found no variations in the depth and the shape of the 3.4 microns organics feature. Hence, the effect of space weathering on organics features is not so clear but it could be expected that these bands disappeared with space weathering.

We compared also the MIX #6 spectrum with other space and ground-based observations of Phobos (Table 4 and Fig. 7). We focused on the comparison, in particular, with spectral slopes and reflectance. It is interesting to note that the concave behavior of the Phobos spectrum near 1 µm is particularly well reproduced with the MIX #6. Whereas the 1.5-2.4 µm spectra slope seems to be quite constant between the different observations, the spectral slope between 720 and 900 nm varies from 9 to 15 %/100nm. Three Phobos spectra are available after 2.5 µm for comparison with MIX #6 in this spectral range. CRISM spectrum (Fraeman et al. 2012) is probably not physical after 2.5 µm and is affected by calibration artifacts. IRTF spectrum from Takir et al. (2022) is redder at these wavelengths but it is impossible to make a definitive conclusion given the poor signal-to-noise ratio whereas IRTF spectrum from Rivkin et al. (2002) is in good agreement within error bars with MIX #6 spectrum.

However, as discussed in Poggiali et al. (2022), the near-infrared spectrum alone is not sufficient to understand the composition of Phobos using a near-infrared simulant. In this context, we investigated the behavior of our visible/near-infrared simulant in the mid-infrared.

3.2 In the MIR

The MIR range gives additional possibilities for the interpretation of the spectra. For Phobos, the MIR spectrum and its interpretation are particularly discussed in Giuranna et al. (2011), Glotch et al. (2018), and Poggiali et al. (2022). Therefore, we compared the spectral features of Phobos in the MIR with the MIX #6 described in this paper.

Because the purpose here is to do a qualitative study in the MIR, we converted our reflectance spectra to emissivity (neglecting diffusion) using Kirchoff's law: $E = 1 - R$, where R is the reflectance and E is the emissivity (Salisbury et al. 1994). We compared our MIX #6 spectrum with spectra from PFS observations (Giuranna et al. 2011), from TES observations (Glotch et al. 2018), and with the UTPS-TB simulant (Miyamoto et al. 2021) as reported in Fig. 8. It seems that MIX #6 has a similar maximum near 12 µm to PFS observations (orbit 5851 and 5870). This feature is shifted towards smaller wavelengths in the case of our simulant compared to PFS observations. Considering spectra of pure endmembers available in Appendix C, these feature is due to olivine in our MIX #6 spectrum. It appears that broad and deep features at 9.5 and 10.7 µm in MIX #6 are due to the presence of olivine in the MIX #6 composition. More precisely, these features are Reststrahlen features (RB, Salisbury et al. 1991). Positions of the RB are slightly dependent on the Mg/Fe ratio (Salisbury et al. 1991). Compared to pure olivine spectra, these features are severely reduced by opaque materials, but not completely removed as for the 1 µm band (see Sect. 3.1).

These two features are not present in the TES and PFS Phobos spectra although in the latter the S/N between 10 and 14 µm is low. Olivine RB is particularly important and persistent even for fine-grained materials (Salisbury et al. 1991), so the non-detection, in particular for the TES observations, of such RB could imply that Phobos is not composed of olivine.

Table 4. Comparison of spectral parameters of the MIX #6 with space and ground-based observations of Phobos. A hyphen in the Table signifies that there is no data at this wavelength for the observation. Uncertainties on the spectral slope and reflectance measurements for the MIX #6 are due to SHADOWS uncertainties. The spectral slope is given in %/100nm.

Spectral params./Obs.	MIX #6	Phobos2/VSK KRFM ISM Murchie & Erard (1996)	MRO/CRISM Fraeman et al. (2012)	IRTF/SpeX Takir et al. (2022)
Spectral slope				
720-900 nm	5.18 ± 0.02	11.31 ± 0.30	8.78 ± 0.45	15.20 ± 1.59
1.5-2.4 µm	2.24 ± 0.10	2.02 ± 0.85	2.99 ± 0.52	2.60 ± 0.67
3.7-4.0 µm	1.88 ± 0.07	–	–	1.62 ± 5.11
Reflectance				
600 nm	0.039 ± 0.001	0.064	0.025	–
1.8 µm	0.057 ± 0.001	0.128	0.049	–
4.0 µm	0.083 ± 0.002	–	–	–
Phase angle of meas./obs.	30°	0° (reprojected)	30° (reprojected)	23.42°

Overtone/combination tone bands can also be seen (Fig. C1) between 4.5 and 6.5 µm (Salisbury et al. 1991) and are completely suppressed by the darkening agent in the MIX #6 spectrum. Fig. C1 in Appendix C shows that the spectral slope between 1.25 and 20 µm is mainly guided by the darkening agent (anthracite). Some spectral features of the anthracite are also visible in the MIX #6 spectrum. Pure DECS-19 spectrum presents several important stretching absorption bands at 6.22 µm and 6.88 µm, but also bending bands due to aromatic cycle (Vinogradoff et al. 2021) between 11 and 14 µm (Fig. C1). Overall, these aromatic bands are also suppressed by the darkening agent. Organic stretching bands at 6.22 and 6.88 µm are not clearly seen in the MIX #6 spectrum and water absorption in the spectrum between 5 and 8 µm complicates the task of absorption band identification. However, the third bending band at 13 µm can still be observed clearly (Fig. C1). The broad and very deep band at 16.6 µm in the observation of orbit 0756 is not observed in MIX #6 as well as in the UTPS-TB.

Investigating the position of the Christiansen feature (CF) gives clues about the mineralogy of Phobos (Salisbury & Walter 1989; Salisbury et al. 1991). From Fig. 8, we clearly observed the CF at 7.9 µm in the simulant emissivity. The position of this feature indicates a match with basaltic materials, volcanic rocks, and feldspar (Salisbury & Walter 1989; Cooper et al. 2002). Giuranna et al. (2011) and Glotch et al. (2018) have found that the CF for Phobos is between roughly 8.4 and 9 µm. At this wavelength, a CF is attributed to ultramafic and meteoritic materials (Salisbury & Walter 1989).

The MIX #6 is, hence, not a really good simulant in the MIR considering the few MIR observations of Phobos. In its paper, Giuranna et al. (2011), found a good match of the PFS spectra with phyllosilicate materials although the variability in the data collected can be also related to compositional inhomogeneity of the Phobos surface. Dehydrated phyllosilicates were also claimed in Fraeman et al. (2014) to explain the observed 0.65 µm and 2.8 features, in ground-based observations. Therefore, for further investigations, the development of a spectral simulant containing phyllosilicates could be useful to improve the match in the mid-infrared region.

3.3 Physical properties of the MIX #6

As described earlier (Sect. 2.3), SEM images were performed on the mixture. By analyzing SEM images of the MIX #6 we are able to improve our knowledge of the mixture's physical properties. Indeed, grain size has an important impact on light propagation, and hence, on the final spectrum appearance. The effect is particularly crucial for the dispersion of the submicron opaques on spectra (Cloutis et al. 1990a,b; Sultana et al. 2021). In the MIX #6 (Fig. B2/9, Appendix B), grains seem to be quite well mixed. Fine-grained opaques are sometimes stuck on larger silicate grains, which is normal behavior in mixing components with different grain sizes.

3.4 The effects of the geometry of observation

In addition to the spectrum acquired in different wavelength domains, the study of different observational geometries can give us information about the effect of the surface texture, the grain size, and other physical properties (Schröder et al. 2014; Fornasier et al. 2015; Pilorget et al. 2016; Potin et al. 2019), and can help the comparison with the few Phobos data available. Moreover, even if small phase angles future observations of MIRS should be favored to have a better S/N, also some measurements at different phase angles will be performed. In this context, it is important to explore the effect of geometry on Phobos simulants for a better interpretation of the MIRS spectra. Using the SHADOWS spectro-goniometer, we acquired 71 spectra of the MIX #6 with different geometries, from phase angles of 0° to 130°. It is interesting to note that, depending on the phase angles, the surface of the MIX #6 observed by SHADOWS can be different. This is due to the widening of the spot as the phase angle increases. The incident angle varies from 0 to 60° with a step of 20°, the emission angle from -70° to 70° with a step of 10°, and the azimuth angle is set to 0°. We acquired also data with an azimuth of 30°, emission angle from -70° to 70°, and with incidence fixed to 0°. In this work, we focussed the study on the effect of the two important spectroscopic parameters described in Sect. 2.5: the spectral slope and the reflectance level. Fig. 9 presents the results of this investigation.

We noticed a relation between spectral slope and phase angle. The presence of phase reddening (i.e., increase of the spectral slope with the phase angle) on Phobos has already been discussed in Pajola et al. (2012) and Wargnier et al. (2023). Compared to the simulant used in Wargnier et al. (2023), the spectral slope is more dispersed, especially at large phase angles. Phase reddening is not a really well-understood phenomenon, but the dispersion of phase reddening could be due to the absence of really small transparent particles (submicron) in the MIX #6 mixture that forward-scattered the light (Schröder et al. 2014). A linear fit of the spectral slope data computed between 1.5 and 2.4 µm as a function of the phase angle gives a slope of the phase reddening of 0.0015 ± 0.0005 $\mu m^{-1}/°$ (sometimes known as the γ parameter for phase reddening). Considering the different Phobos' spectroscopic observations that were performed at different

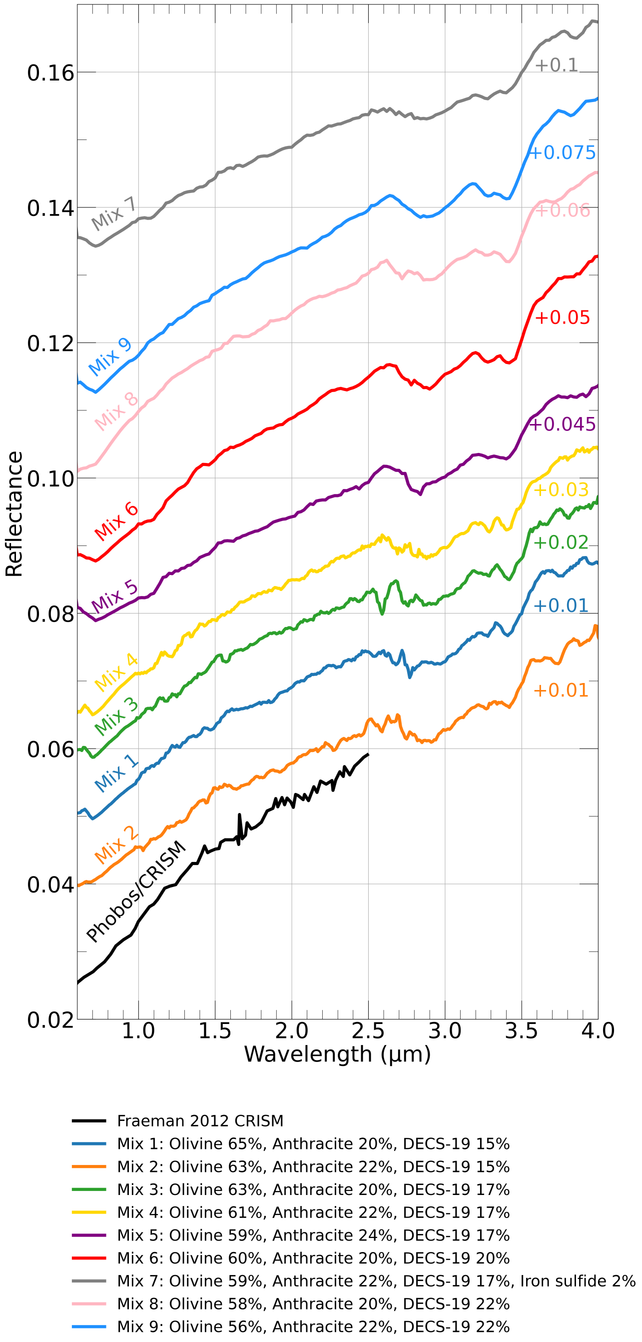

Figure 4. SHADOWS spectra of the different mixtures prepared in this work. We added an offset on the spectra in order to see all the spectra and to compare the spectral slope of the different mixtures with the Phobos' data from Fraeman et al. (2012). Spectra presented in this figure are smoothed using a moving average on five points.

phase angles, we can compute a γ factor for Phobos. Using data available between 1.5 and 2.4 µm for Phobos from Murchie & Erard (1996) (reprojected, $\alpha = 0°$), Fraeman et al. (2012) ($\alpha = 63°$ for OMEGA data and $\alpha = 41°$ for CRISM data), and Takir et al. (2022) ($\alpha = 23.42°$); we found a γ value of 0.0012 ± 0.0004 $\mu m^{-1}/°$. The phase reddening coefficient of Phobos is, hence, in agreement with the value measured in our MIX #6, taking into account associated uncertainties. Phase reddening effects were detected on several small

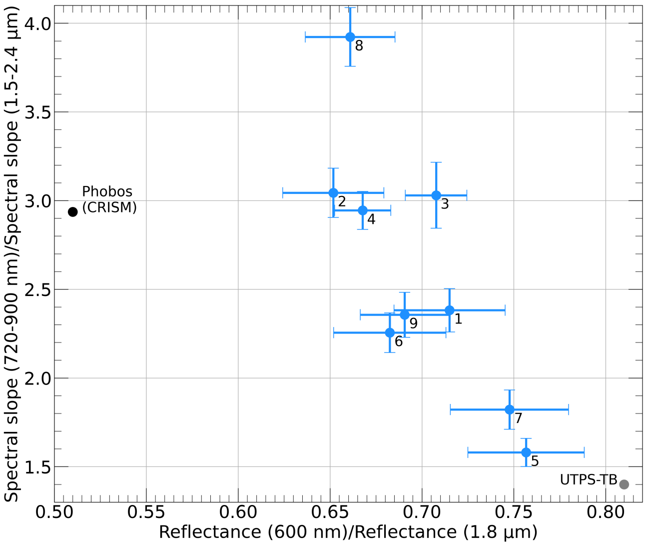

Figure 5. Ratio of the spectral slope between 720 and 900 nm to the spectral slope between 1.5 and 2.4 µm as a function of the ratio of the reflectance at 600 nm to the reflectance at 1.8 µm. The black point represents the Phobos CRISM data and the gray point the Univ. Tokyo Phobos Simulant-Tagish based Phobos simulant (UTPS-TB) data, respectively derived from Fraeman et al. (2012) and Miyamoto et al. (2021). Blue points are related to mixtures prepared in this work (see Table 1). Uncertainties are computed by error propagation on the SHADOWS measurements. Numbers correspond to the mixture number given in Table 1.

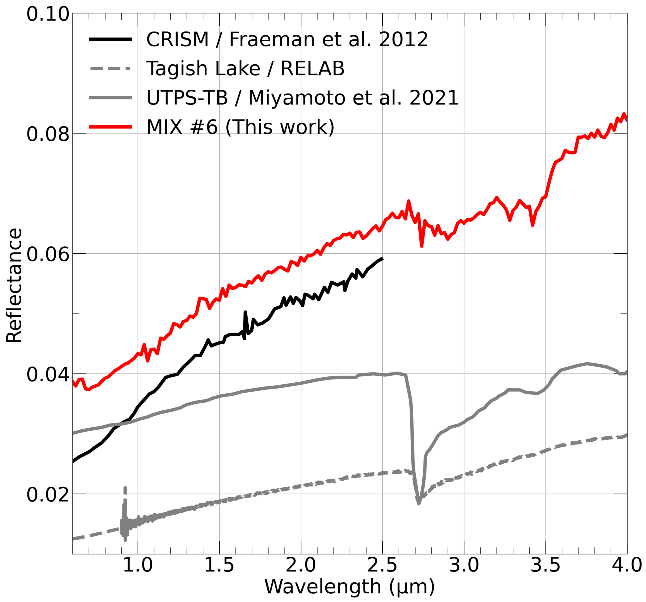

Figure 6. SHADOWS spectrum of the Phobos spectral simulant (MIX #6) developed in this work, from 0.6 µm to 4.2 µm. Comparison of the spectrum with the Phobos CRISM spectrum (Fraeman et al. 2012), with Tagish Lake meteorite spectrum, and with spectrum of the Univ. Tokyo Phobos Simulant (UTPS, Miyamoto et al. 2021). UTPS spectrum was digitized from the original paper. UTPS-TB is a Tagish-based Phobos simulant. The reader can refer to Miyamoto et al. (2021) for the composition and the characteristics of the simulant. Near-infrared Tagish Lake spectrum is obtained through the RELAB database and corresponds to a 0-125 µm weathered portion of the meteorite. The part of the spectrum between 0.6 and 0.9 is extrapolated.

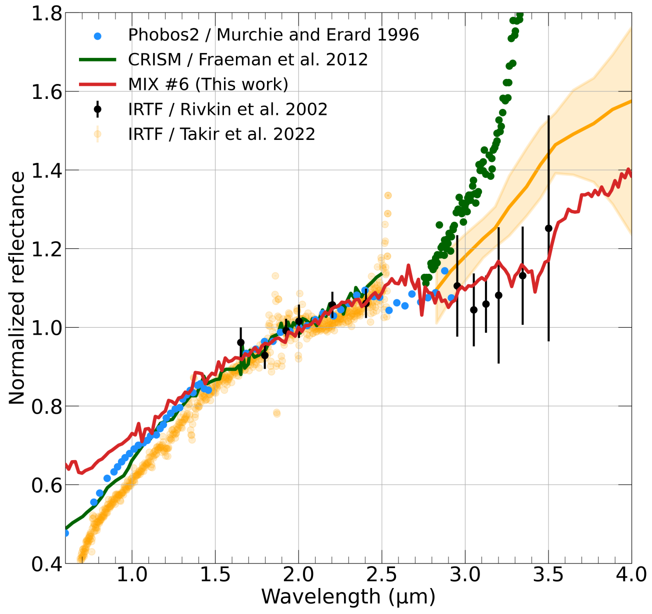

Figure 7. SHADOWS spectrum of the Phobos spectral simulant (MIX #6) developed in this work, from 0.4 µm to 4.2 µm. Comparison of the spectrum with space and ground-based observations (CRISM, Phobos2/VSK, and IRTF). Reflectance is normalized at 2.0 µm. Spectra are digitized from the original papers specified on the label. Takir's spectrum between 2.8 and 4.0 µm was obtained in Takir et al. (2021). The orange straight line is the mean value obtained in the paper. The orange-shaded region represents the uncertainty associated with Takir's measurements. CRISM spectrum of Phobos after 2.7 µm is probably not physical and according to Fraeman et al. (2012) the spectrum is affected by radiometric calibration artifacts at these wavelengths.

bodies including the comet 67P/Churyumov-Gerasimenko, Bennu, Ryugu, and Ceres (Fornasier et al. 2015, 2020; Ciarniello et al. 2015, 2017; Longobardo et al. 2017, 2019, 2022). In particular, comet 67P has a similar albedo and slope to Phobos, and a reddening γ coefficient of 0.0013-0.0018 $\mu m^{-1}/^{\circ}$ in the wavelength region of 1 to 2 µm was reported (Ciarniello et al. 2015; Longobardo et al. 2017). Phase reddening is therefore comparable between 67P, Phobos, and MIX #6 presented in this work for the same spectral range.

Focusing on reflectance, we observed also a clear dependence on the phase angle. It seems there is an increase of the reflectance at large phase angles (i.e., forward-scattering) and at low phase angles. The increase of the reflectance for small phase angles is mainly due to shadow-hiding in our measurements as the backscattering opposition effect is generally invoked for very low phase angles ($<3^{\circ}$). However, Phobos' observations (up to 90°) (Avanesov et al. 1991) with disk-integrated analysis have shown that reflectance decreases with the increase of phase angle. Due to a lack of SHADOWS data for the simulant at very low phase angles ($<10^{\circ}$), we are unable to say whether the coherent-backscattering opposition effect is observed for our sample. It is interesting to note that the incidence angle appears to have an impact on the phase function of the MIX #6. For higher incidence angles but for the same phase angles the reflectance is higher. This effect is particularly important for extreme geometries (e.g., at 10°).

The geometry behavior of our MIX #6 is, therefore, not totally in agreement with the past observations of Phobos but could still offer important information for the interpretation of past and future observations of Phobos. Dependence of the phase angle for reflectance and in particular spectral slope is complicated to estimate for a given material, and it could be even more complicated to find a mixture that fits well with the Phobos' data at different phase angles.

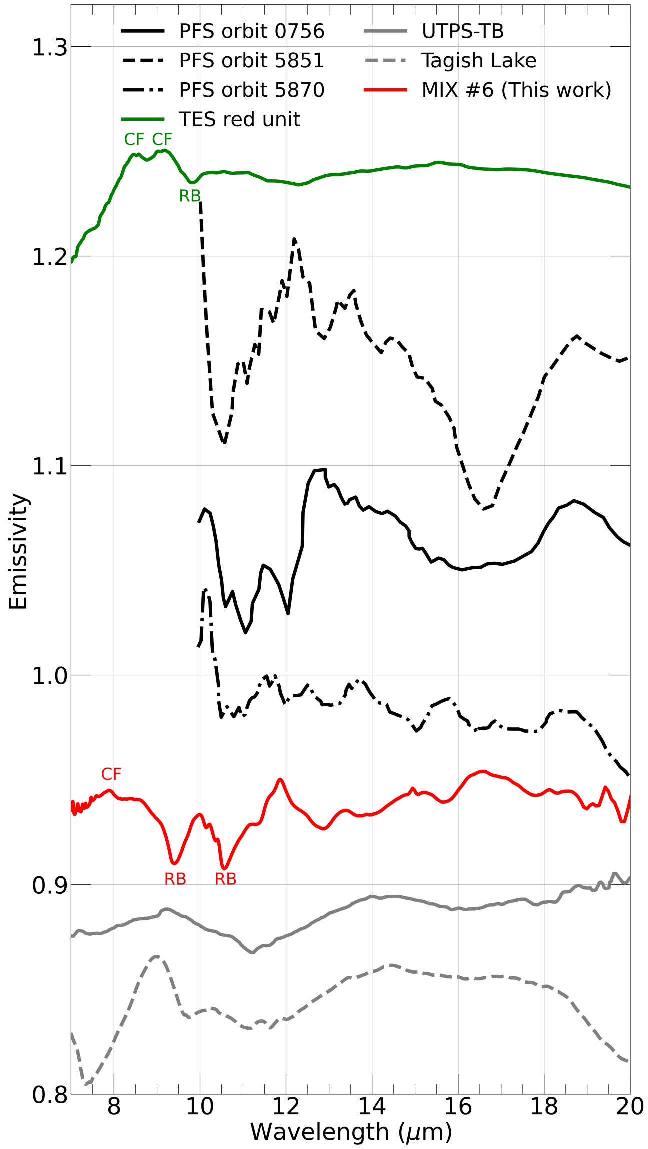

Figure 8. MIR spectra of MIX #6 from this work compared to MIR observations of Phobos: PFS from Giuranna et al. (2011), TES from Glotch et al. (2018), and simulants for Phobos: UTPS-TB simulant proposed by Miyamoto et al. (2021) and Tagish Lake meteorite. Error bars of the PFS observations are reported in Giuranna et al. (2011). The Tagish Lake spectrum was acquired on unsorted dust at ambient temperature and nitrogen atmosphere in INAF – Astrophysical Observatory of Arcetri laboratory. Laboratory spectra were acquired in reflectance and converted in emissivity using Kirchoff's law. Offsets were added for clarity reasons.

4 CONCLUSIONS

The development of a spectral simulant of Phobos is a strenuous task as the knowledge about the composition of Phobos is still uncertain. The MMX mission and, in particular, the MIRS spectrometer

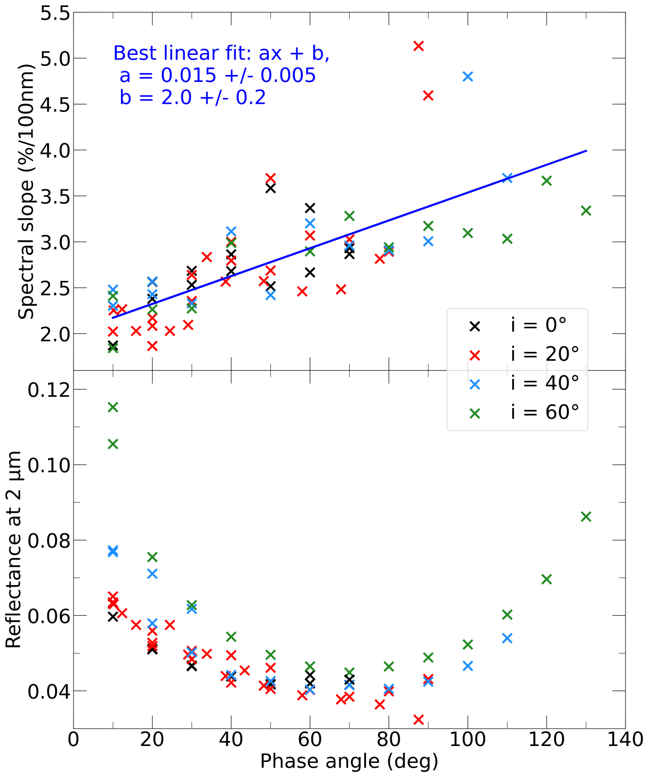

Figure 9. Spectral slope and reflectance as a function of phase angle. The spectral slope is given in %/100nm and was computed between 1.5 and 2.4 µm for each spectrum. Reflectance is computed at 2 µm.

(Barucci et al. 2021), will be precious to investigate and constrain the Phobos surface composition.

Our results show that we were able to develop a good visible and near-infrared spectroscopic simulant of Phobos. This simulant was obtained by mixing olivine (60 vol.%), anthracite (20 vol.%), and DECS-19 (20 vol.%, coal from the Penn State Coal Sample Bank). This mixture composed of silicate and coal materials could be representative of a possible composition for Phobos according to the hypothesis of a captured D-type small body. The presence of opaques materials is responsible for the removal of the 1 µm olivine absorption feature. However, the spectrum in the mid-infrared is not fully consistent with Phobos observations. Indeed, it is particularly challenging to obtain spectra that fit well the Phobos' data in all the wavelength ranges from visible to mid-infrared due to the lack of knowledge on compositional information about Phobos and the absence of features. Geometry effects observed on Phobos on reflectance and spectral slope are also partially observed with our simulant.

For further investigations, according to Giuranna et al. (2011), the use of phyllosilicates could be useful to improve the match of Phobos spectrum in the mid-infrared. The red and flat spectrum could also be explained by the space weathering including solar wind, galactic cosmic rays, and – because Phobos is close to Mars – sputtering of Mars atmospheric particles (Nénon et al. 2019, 2021). Therefore, irradiation of Phobos simulants should be realized.

ACKNOWLEDGEMENTS

This work was carried out in support for the MIRS instrument onboard the future MMX mission, with the financial support of the Centre National d'Etudes Spatiales (CNES). T.G. and A.W. acknowledge fundings from Agence Nationale de la Recherche under the grant ANR-20-CE49-0004-01. We warmly thank the anonymous reviewer for the precious comments and suggestions that contributed to improve the manuscript.

DATA AVAILABILITY

Data will be available on the SSHADE database (Solid Spectroscopy Hosting Architecture of Databases and Expertise). The data will be also shared on reasonable request to the corresponding author.

REFERENCES

Avanesov G., et al., 1991, Planet. Space Sci., 39, 281
Barucci M. A., et al., 2021, Earth, Planets and Space, 73, 211
Beck P., Schmitt B., Potin S., Pommerol A., Brissaud O., 2021, Icarus, 354, 114066
Bishop J., Pieters C., Mustard J., Pratt S., Hiroi T., 1994, Meteoritics, 29, 444
Brucato J. R., Migliorini A., Barucci M. A., Carvano J. M., Dotto E., Mennella V., 2010, A&A, 516, A92
Brunetto R., et al., 2014, Icarus, 237, 278
Buhl E., Sommer F., Poelchau M. H., Dresen G., Kenkmann T., 2014, Icarus, 237, 131
Ciarniello M., et al., 2015, A&A, 583, A31
Ciarniello M., et al., 2017, A&A, 598, A130
Cloutis E. A., Gaffey M. J., Smith D. G. W., Lambert R. S. J., 1990a, Icarus, 84, 315
Cloutis E. A., Gaffey M. J., Smith D. G. W., Lambert R. S. J., 1990b, J. Geophys. Res., 95, 281
Cooper B. L., Salisbury J. W., Killen R. M., Potter A. E., 2002, Journal of Geophysical Research (Planets), 107, 5017
Craddock R. A., 1994, in Lunar and Planetary Science Conference. Lunar and Planetary Science Conference. p. 293
Craddock R. A., 2011, Icarus, 211, 1150
Delsanti A. C., Boehnhardt H., Barrera L., Meech K. J., Sekiguchi T., Hainaut O. R., 2001, A&A, 380, 347
Fanale F. P., Salvail J. R., 1989, Geophysical Research Letters, 16, 287
Fanale F. P., Salvail J. R., 1990, Icarus, 88, 380
Flinn D., 1983, Geological Journal, 18, 277
Fornasier S., et al., 2015, A&A, 583
Fornasier S., et al., 2020, A&A, 644, A142
Fraeman A. A., et al., 2012, Journal of Geophysical Research (Planets), 117, E00J15
Fraeman A. A., Murchie S. L., Arvidson R. E., Clark R. N., Morris R. V., Rivkin A. S., Vilas F., 2014, Icarus, 229, 196
Giuranna M., Roush T. L., Duxbury T., Hogan R. C., Carli C., Geminale A., Formisano V., 2011, Planet. Space Sci., 59, 1308
Glotch T. D., Edwards C. S., Yesiltas M., Shirley K. A., McDougall D. S., Kling A. M., Bandfield J. L., Herd C. D. K., 2018, Journal of Geophysical Research (Planets), 123, 2467
Godard M., et al., 2011, A&A, 529, A146
Hyodo R., Genda H., Charnoz S., Pignatale F. C. F., Rosenblatt P., 2018, ApJ, 860, 150
Just G. H., Joy K. H., Roy M. J., Smith K. L., 2020, Acta Astronautica, 173, 414
Koike C., Shibai H., Tuchiyama A., 1993, Monthly Notices of the Royal Astronomical Society, 264, 654
Kuramoto K., et al., 2022, Earth, Planets and Space, 74, 12
Landsman Z. A., Schultz C. D., Britt D. T., Peppin M., Kobrick R. L., Metzger P. T., Orlovskaya N., 2021, Advances in Space Research, 67, 3308

Lantz C., et al., 2015, A&A, 577, A41

Longobardo A., et al., 2017, MNRAS, 469, S346

Longobardo A., et al., 2019, Icarus, 320, 97

Longobardo A., et al., 2022, A&A, 666, A185

Lunine J. I., Neugebauer G., Jakosky B. M., 1982, J. Geophys. Res., 87, 10297

Miyamoto H., et al., 2021, Earth, Planets and Space, 73, 214

Murchie S., 1999, J. Geophys. Res., 104, 9069

Murchie S., Erard S., 1996, Icarus, 123, 63

Nénon Q., Poppe A. R., Rahmati A., Lee C. O., McFadden J. P., Fowler C. M., 2019, Journal of Geophysical Research (Planets), 124, 3385

Nénon Q., Poppe A. R., Rahmati A., McFadden J. P., 2021, Nature Geoscience, 14, 61

Pajola M., et al., 2012, MNRAS, 427, 3230

Pajola M., Roush T., Dalle Ore C., Marzo G. A., Simioni E., 2018, Planetary and Space Science, 154, 63

Pätzold M., Andert T. P., Jacobson R., Rosenblatt P., Dehant V., 2013, in European Planetary Science Congress. pp EPSC2013–901

Pilorget C., Fernando J., Ehlmann B. L., Schmidt F., Hiroi T., 2016, Icarus, 267, 296

Poggiali G., et al., 2022, MNRAS, 516, 465

Potin S., Brissaud O., Beck P., Schmitt B., Magnard Y., Correia J.-J., Rabou P., Jocou L., 2018, Appl. Opt., 57, 8279

Potin S., Beck P., Schmitt B., Moynier F., 2019, Icarus, 333, 415

Potin S. M., Douté S., Kugler B., Forbes F., 2022, Icarus, 376, 114806

Rivkin A. S., Brown R. H., Trilling D. E., Bell J. F., Plassmann J. H., 2002, Icarus, 156, 64

Rosenblatt P., Charnoz S., Dunseath K. M., Terao-Dunseath M., Trinh A., Hyodo R., Genda H., Toupin S., 2016, Nature Geoscience, 9, 581

Sakatani N., Ogawa K., Arakawa M., Tanaka S., 2018, Icarus, 309, 13

Salisbury J. W., Walter L. S., 1989, J. Geophys. Res., 94, 9192

Salisbury J. W., D'Aria D. M., Jarosewich E., 1991, Icarus, 92, 280

Salisbury J. W., Wald A., D'Aria D. M., 1994, J. Geophys. Res., 99, 11897

Schneider C. A., Rasband W. S., Eliceiri K. W., 2012, Nature Methods, 9, 671

Schröder S. E., Grynko Y., Pommerol A., Keller H. U., Thomas N., Roush T. L., 2014, Icarus, 239, 201

Simon J. I., et al., 2018, Earth and Planetary Science Letters, 494, 69

Singer R. B., 1981, J. Geophys. Res., 86, 7967

Sultana R., Poch O., Beck P., Schmitt B., Quirico E., 2021, Icarus, 357, 114141

Sultana R., et al., 2023, Icarus, 395, 115492

Takir D., Stockstill-Cahill K. R., Hibbitts C. A., Nakauchi Y., 2019, Icarus, 333, 243

Takir D., Matsuoka M., Waiters A., Kaluna H., Usui T., 2021, in 52nd Lunar and Planetary Science Conference. Lunar and Planetary Science Conference. p. 1386

Takir D., Matsuoka M., Waiters A., Kaluna H., Usui T., 2022, Icarus, 371, 114691

Thomas N., Britt D. T., Herkenhoff K. E., Murchie S. L., Semenov B., Keller H. U., Smith P. H., 1999, J. Geophys. Res., 104, 9055

Toriumi M., 1989, Earth and Planetary Science Letters, 92, 265

Vinogradoff V., et al., 2021, Minerals, 11, 719

Wargnier A., et al., 2023, A&A, 669, A146

APPENDIX A: SPECTRAL PARAMETERS WITH SHADOWS

Parameters set for measurements with SHADOWS are presented in this appendix. The spectral sampling is 20 nm for most of the sample except for olivine where we used a spectral sampling of 50 nm. Spectral resolution depends on the wavelength. It is smaller for shorter wavelengths as shown in Fig. A.

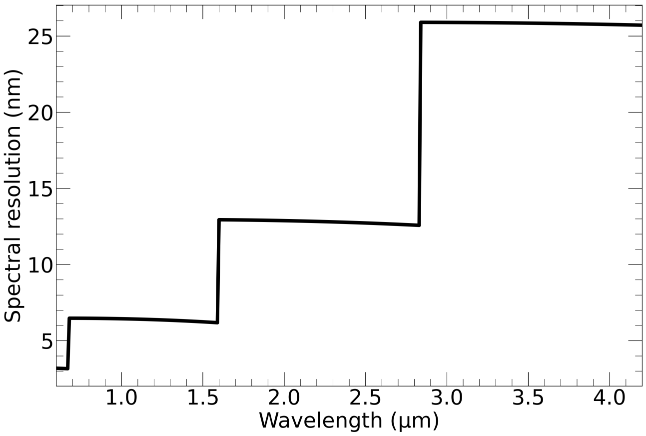

Figure A1. Spectral resolution used with SHADOWS as a function of the wavelength.

APPENDIX B: SEM IMAGES

Fig. B1/1 and Fig. B1/2 are SEM images of the olivine pure sample. Fig. B1/3 Fig. B1/4 and Fig. B1/5 are SEM images of the hyperfine pure anthracite sample. Fig. B2/6, Fig. B2/7, and Fig. B2/8 are SEM images of the pure DECS-19 sample.

Fig. B2/9 and Fig. B2/10 are SEM images of the MIX #6.

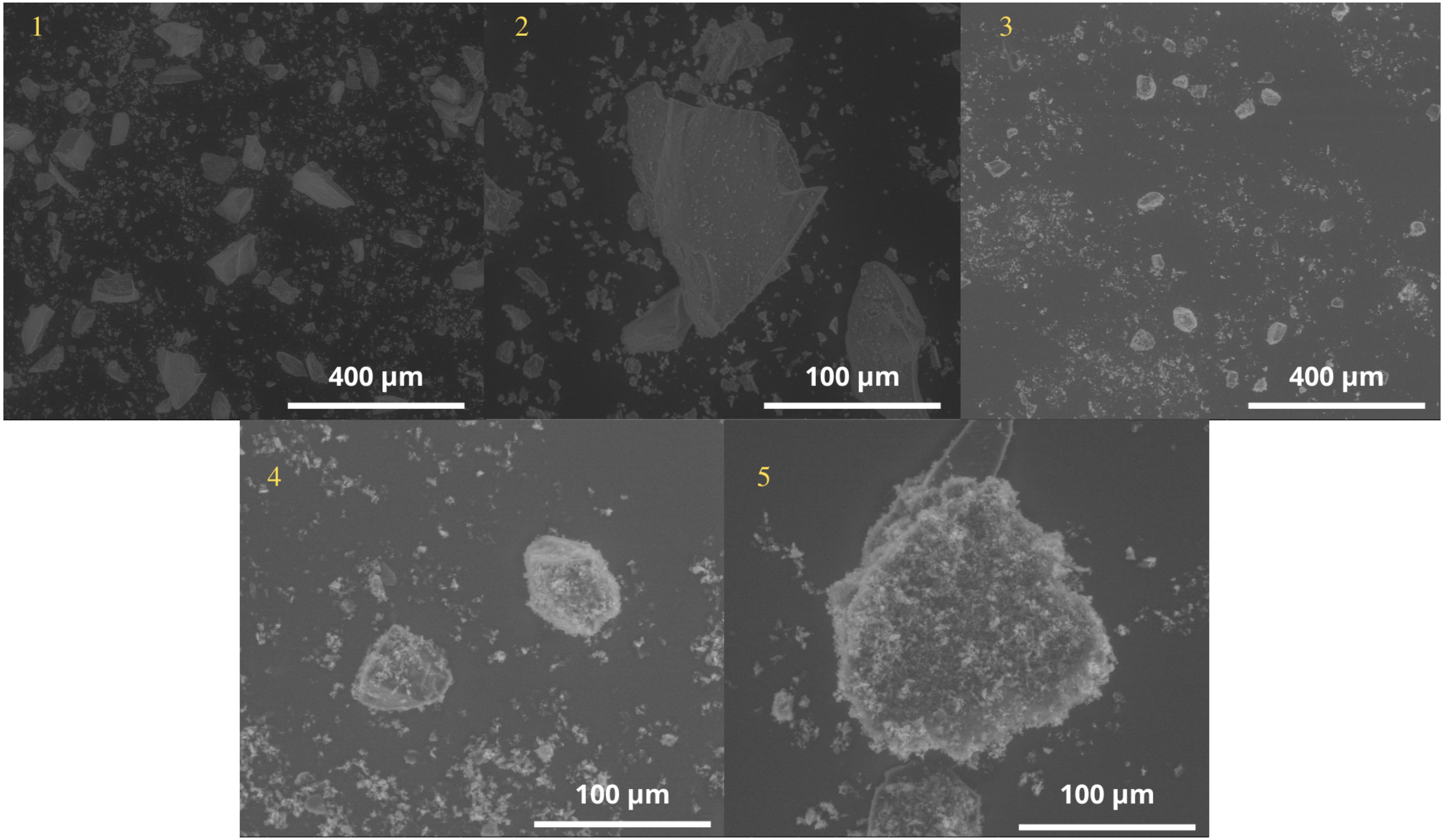

Figure B1. 1: SEM image of the olivine sample with a magnification of 250. This general view allows seeing the diversity of olivine grain size with a grain size of more than 250 µm and really small grains. **2:** SEM image of the olivine sample with a magnification of 1000. This view permits us to see the presence of olivine dust on the big grain. **3:** SEM image of the anthracite sample with a magnification of 250. We observed that anthracite is more homogeneous than olivine in terms of grain size. However, some grains remain quite big and fine-grain are sometimes clumped together. **4:** SEM image of the anthracite sample with a magnification of 1000. **5:** SEM image of the anthracite sample with a magnification of 1000.

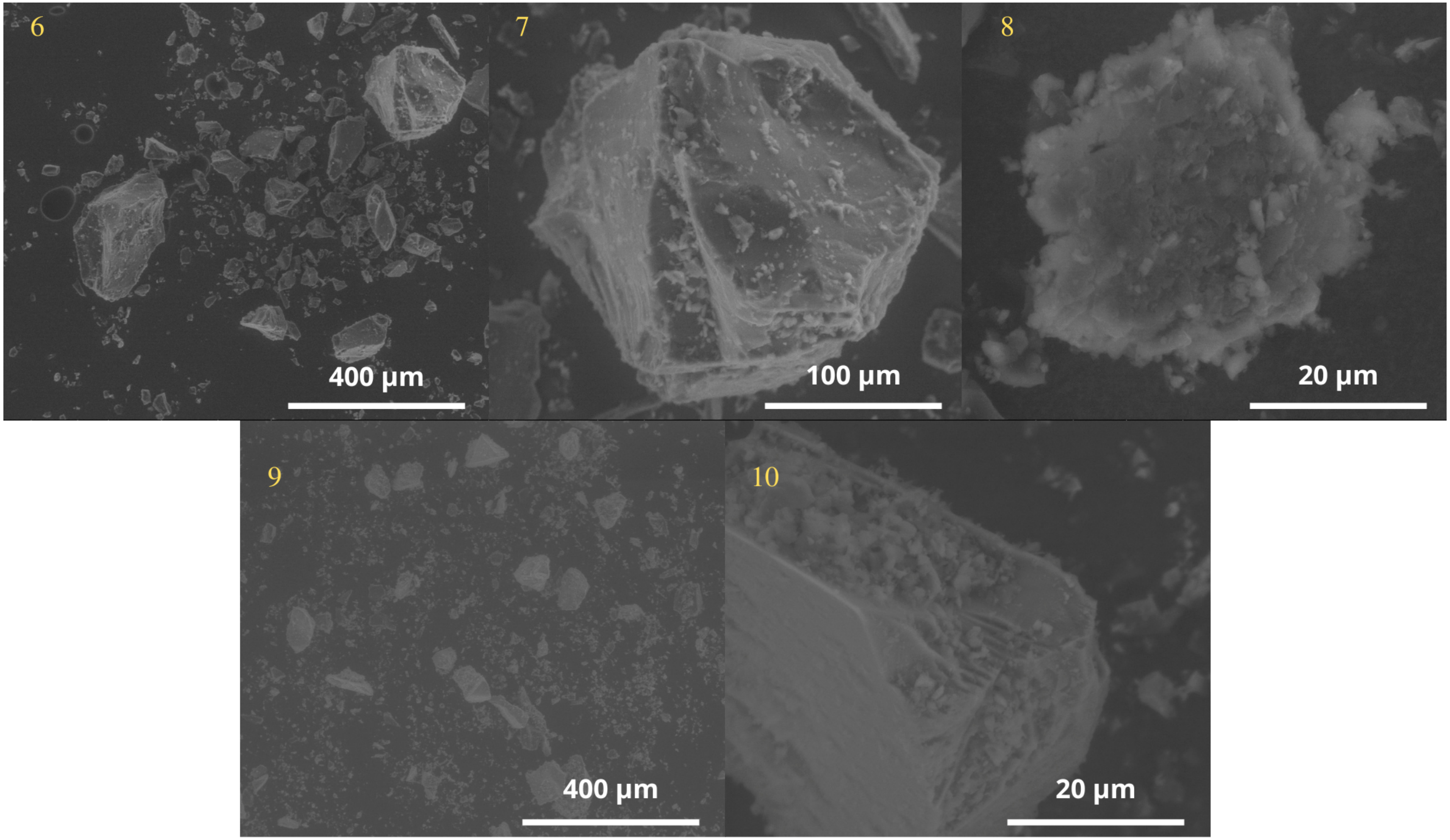

Figure B2. **6:** SEM image of the DECS-19 sample with a magnification of 250. The black circles in the images are artifacts caused by the carbon tape under the sample. **7:** SEM image of the DECS-19 sample with a magnification of 1000. **8:** SEM image of the DECS-19 sample with a magnification of 4000. **9:** SEM image of the MIX #6 with a magnification of 250. **10:** SEM image of the MIX #6 with a magnification of 4000.

APPENDIX C: SPECTRA OF PURE END-MEMBERS IN THE MIR

This appendix presents the end-members spectra – olivine, anthracite, and DECS-19 – of the MIX #6 in the near- and mid-infrared (2 - 20 µm) measured using materials presented in Sect. 2.4 (see Fig. C1).

This paper has been typeset from a TEX/LATEX file prepared by the author.

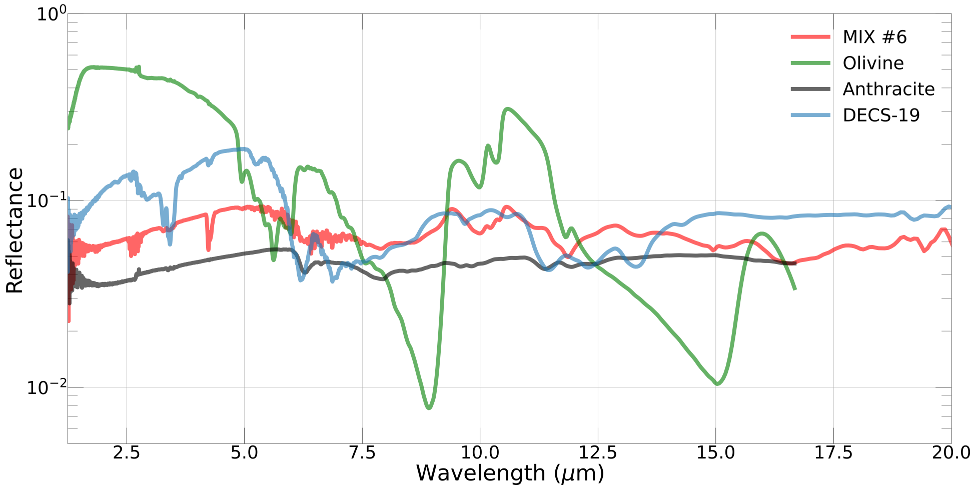

Figure C1. MIR reflectance spectra of pure endmembers of the MIX #6 compared to the MIX #6 spectrum. In particular, note the position of the different absorption bands.